Response of Hurricane Harvey's rainfall to anthropogenic aerosols: A sensitivity study based on spectral bin microphysics with simulated aerosols

Amir H. Souri[a,b,*], Yunsoo Choi[a], John K. Kodros[c], Jia Jung[a], Jacob Shpund[d], Jeffrey R. Pierce[c], Barry H. Lynn[d], Alexander Khain[d], Kelly Chance[b]

[a] Department of Earth and Atmospheric Sciences, University of Houston, Houston, TX, USA
[b] Harvard-Smithsonian Center for Astrophysics, Cambridge, MA, USA
[c] Department of Atmospheric Science, Colorado State University, Fort Collins, CO, USA
[d] The Institute of Earth Sciences, The Hebrew University of Jerusalem, IL, Israel

A B S T R A C T

A number of human-induced elements contribute to influencing the intensity of tropical cyclones and prolonging their lifetime. Not only do ocean heat content, large-scale weather patterns, and surface properties affect the amount of release of energy, but the modulation from aerosol particles on cloud properties is also present. With Hurricane Harvey (2017) fairly isolated over Texas, there was a unique opportunity to study the indirect impact of aerosols on the amount of record-breaking rainfall over the greater Houston area. Due to the non-linear processes involved in clouds microstructure, aerosol properties and the variability associated with the atmospheric environment, the quantification of the response of storms to aerosols is complex. To this end, we first reproduce Harvey using the Weather Research and Forecasting (WRF) model coupled with a 3D-var assimilation framework that incorporates satellites, radio occultation, dropsondes, and surface measurements. We then study the aerosol indirect impacts using spectral bin microphysics in conjunction with aerosol properties simulated from the Goddard Earth Observing System (GEOS)-Chem TwO-Moment Aerosol Sectional (TOMAS) model leveraging online aerosol microphysics with anthropogenic emissions (SP) and without ones (SC). In the vicinity of Harvey's landfall, the number concentration of cloud condensation nuclei at 1% supersaturation using the anthropogenic emissions is found to be one order of magnitude ($855\ cm^{-3}$) larger than those simulated with only natural emissions ($83\ cm^{-3}$). We observed that a narrow plume of anthropogenic aerosols from western Texas was transported over the area at the moment when deep convection initiated, accelerating updrafts through releasing more latent heat, which in turn, resulted in an average enhancement of precipitation by 25 mm ($\sim$ 8%) over the greater Houston area. We observed a second peak at the right tail of the distribution of differences between experiments, which is an indication of the presence of more extreme rainfall over the area. As such, studies on the impact of aerosol emissions controls on exacerbating severe weather should be more encouraged.

1. Introduction

Hurricanes play an essential part of the Earth's energy balance by distributing excess energy to higher latitudes. Since year-to-year oscillations in their frequency and intensity are large, adaptation to this natural hazard has always been a challenge for humans. Due to scarcity of historical observations of hurricanes before the time when the global view of the Earth from satellites has been available, little is known about their overall trends. Nonetheless, having reasonable knowledge of their dynamical structure and interactions with the atmospheric environment embedded in numerical weather models permits the quantification of their responses to a number of variables such as sea surface temperature (Emanuel, 1986; Lin et al., 2015), greenhouse gases (Knutson et al., 2010), and aerosols (Khain et al., 2005; Lynn et al., 2015; Wang et al., 2014b; Yang et al., 2018; Zhao et al., 2018).

Assuming that tropical cyclones follow a Carnot cycle, their thermodynamic efficiency can be calculated through the ratio of work done against friction in the boundary layer to the total heat gain from oceans. This ratio is proportional to the difference between the temperature at the surface (source of energy) and that in the upper atmosphere (loss of heat) (Emanuel, 1987). This indicates that a warmer ocean can increase the temperature difference, resulting in stronger winds and larger azimuthal surface stress, thereby enhancing precipitation (Lu et al., 2018). For example, using satellite-derived precipitation measurements and a high-resolution global atmospheric model, Lin et al. (2015) found a positive slope between the sea surface temperature and the rainfall rate generated from different tropical cyclones occurring between 1981 and 2005. The radiative forcing induced by greenhouse gases might also increase the intensity of hurricanes (Knutson et al., 2010; Walsh et al., 2016), as the principle of Clausius-Clapeyron relation proves that a warmer air possesses larger water vapor capacity (Hartmann et al., 2010). The consequences of having a warmer climate, however, are not limited to having an excess heat content. Kossin (2018) found that, on average, the translation speed of tropical cyclones decreased by 10%
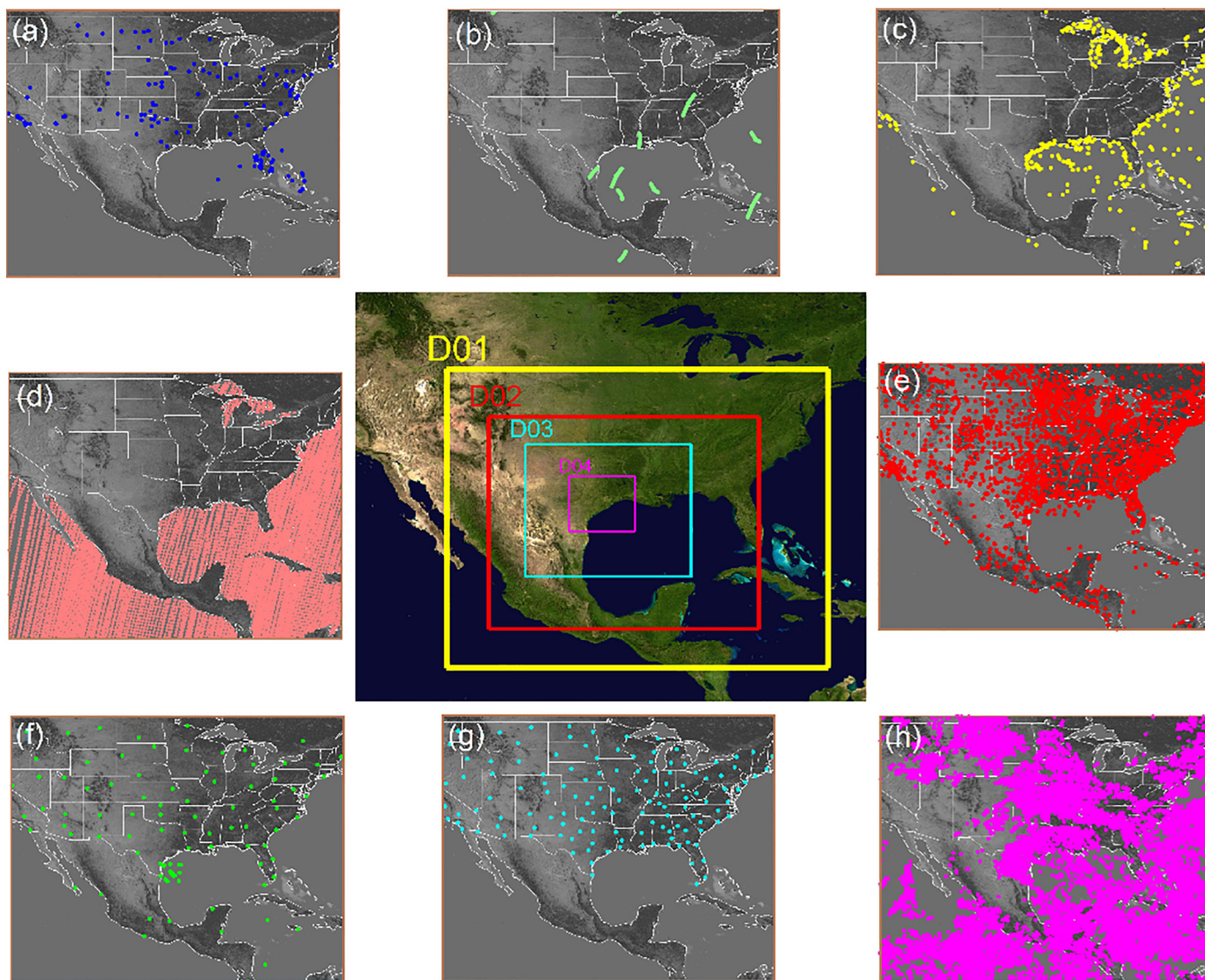
Fig. 1. A snapshot of the locations of available observations that were used for the WRFDA at 1200 UTC 25 August 2017: (a) aircraft, (b) GPS radio occultation, (c) surface marine, (d) microwave satellite radiance, (e) surface land, (f) upper-air, (g) wind profiler, and (h) satellite-derived wind vectors. The central panel shows the 4 spatial domains used in the WRF modeling.

between 1949 and 2016, attributed to the reduction of summertime tropical circulation, which was possibly caused by global warming. In response, a relatively longer time is given to hurricanes to consume moisture/latent energy from oceans.

In addition to gas-phase radiative forcing, aerosols can directly affect the solar radiation (Jung et al., 2019; Kochanski et al., 2019), long-wave radiation (Garrett and Zhao, 2006), and act as cloud condensation nuclei (CCN) potentially perturbing the thermodynamics associated with clouds (Albrecht, 1989; Tao et al., 2012). Since explicitly solving the cloud microstructure is computationally burdensome and the precise knowledge of aerosol properties is limited, the indirect impacts of aerosols on the microphysics of hurricanes (or clouds in general) are relatively less understood. As such, elucidating the response of hurricanes to aerosols heavily relies on the assumptions made for the cloud microphysics scheme and the initial physical/chemical conditions of the atmosphere. Several studies have investigated the response of tropical cyclones to the penetration of aerosols under different simulations and found that aerosols might intensify the periphery (Khain et al., 2008, Khain et al., 2016; Lynn et al., 2015; Wang et al., 2014), or the inner core of a storm (Shpund et al., 2019). Zhao et al. (2018) provided observational evidence of an enhancement of precipitation made by

various tropical cyclones by 4% for an increase of 0.1 aerosol optical depth over the western North Pacific. Lynn et al., 2015 studied hurricane Irene (2011) with the spectral bin microphysics (SBM) scheme (Lynn et al., 2005), which explicitly calculates the activation of aerosols according to the Köhler theory under uniform and non-uniform aerosol distributions. They found that the non-uniform aerosol concentrations inferred from satellite observations could better reproduce the time at which the hurricane began to weaken. This underscores the importance of having reasonable knowledge of characteristics of aerosols including their concentration, size distribution, and solubility to be able to realistically quantify the aerosol-cloud interaction.

The motivation of this study is to investigate the indirect impact of anthropogenic aerosols on Hurricane Harvey (2017) releasing an unprecedented amount of rain over the greater Houston area. Studies done by both Risser and Wehner (2017) and Emanuel (2017) suggested that the likelihood of occurrence of such a currently rare hurricane will increase in a warmer climate; therefore, an understanding of the extent to which anthropogenic aerosols can modulate Harvey's rainfall, which will provide a basis for regulating air pollution, is critical to mitigating the devastating impacts of such events. Since the framework of experiments in this study will be designed in a deterministic way, results

become inevitably subject to both the initial conditions of the atmosphere and the parametrization used for the cloud microphysics. Therefore, to better able to reproduce Harvey (i.e., establishing the ideal initial condition), we will make use of a large suite of observations including satellite and dropsonde measurements; we will improve the initial conditions of our simulation using a variational data assimilation framework. We prefer the SBM scheme over a bulk one because previous studies suggested that the sensitivity of bulk microphysics schemes to aerosol is generally low (Fan et al., 2016 and the references therein; Shpund et al., 2019). Additionally, simulations with a bin microphysical scheme are considered benchmarks in computing aerosol-cloud interactions. Aerosol fields will be simulated by a well-established chemical transport model that will not only provide predictions of necessary aerosol-related inputs for the microphysics scheme, but it also allows for more realistic estimates of the sensitivity of hurricanes to aerosols from different sources (e.g. natural vs. anthropogenic).

In this study, we will i) reproduce Harvey at landfall (i.e., adjusting initial conditions) using a state-of-the-art weather model coupled with a numerical data assimilation framework, ii) simulate the aerosols using a global chemical transport model under different emissions scenarios, and iii) study the sensitivity of Harvey's rainfall to aerosols.

2. Measurements and modeling

2.1. Measurements used for data assimilation

To improve predictions of the numerical model, we used a broad spectrum of data that are composed of surface, profile, and satellite observations. A more detailed description of each will follow:

2.1.1. NCEP ADP global upper air and surface weather observations

The data provide a global set of surface and upper air observations from several sources including surface land, radiosonde, buoy, radar, profiler, and aircraft measurements. Additionally, the data have included atmospheric motion vectors from geostationary satellite observations (Bedka and Mecikalski, 2005) from GOES satellites, which are found to be useful in improving hurricane simulations (e.g., Velden et al., 2016). A snapshot of the spatial distribution of the data is shown in Fig. 1. It is worth noting that dropsondes (> 145 at various hours) near the hurricane (Fig. 1f) have also been included in this dataset.

2.1.2. GPS Radio Occultation (RO) data

Some difficulty in simulating tropical cyclones, particularly the rapid intensification, originates from a lack of an accurate vertical structure of governing variables such as moisture in the low to mid troposphere. Therefore, we complemented the conventional upper air data with GPS radio occultation (RO) refractivity. During an occultation event, the ray between a GPS satellite (emitter) and a low Earth-orbiting one (receiver) is refracted while scanning the atmosphere. The atmospherically bending angles along the trajectory of the ray path under the assumption of spherically symmetric refractivity fields are estimated from the knowledge of precise positions and velocities of the receiver and the emitter (Kursinski et al., 1997). Subsequently, the three-dimensional atmospheric refractivity fields are derived by the Abel transform (Anthes et al., 2008). Since the refractivity is a function of pressure, temperature, and water vapor pressure, these fields from the numerical model are modified with respect to GPS RO.

2.1.3. Microwave satellite radiance

To gain more insights into the vertical distributions in temperature and water vapor mixing ratios at a high spatial coverage, we used microwave satellite radiance (i.e., brightness temperature) from three sensors namely as the Advanced Microwave Sounding Unit-A (AMSU-A) onboard NOAA-15 to NOAA-19, the Microwave Humidity Sounder (MHS) flying on NOAA-18 and NOAA-19, and the Advanced Technology Microwave Sounder (ATMS) onboard NPP. Each of these

polar-orbiting sensors are a cross-track scanner measuring several microwave bands mostly between 89 GHz to 183 GHz at different spatial resolutions (16–85 km nadir pixel) and swath widths. Because of large sensitivities of the microwave bands to relatively uncertain surface land parameters such as soil moisture, we only used the data over water (Fig. 1d). Several quality-control tests were applied to assimilate only qualified pixels (some of which had been included in the data). For instance, we removed those pixels which were contaminated by precipitation based on thresholds defined in Ferraro et al. (2000). The satellite radiance measurements are subject to systematic errors which can induce biases in the final product. Owing to the fact that these errors can vary from sensor to sensor and under different satellite geometric and atmospheric conditions, we first used an offline linear regression (cold start) to mitigate the biases, and then adaptively updated them within a variational minimization known as varBC algorithm (Auligné et al., 2007). Satellite radiance data are spatially correlated, which may sound useful to reduce random noises, but replicates do not enhance the amount of information (i.e., rank of matrix); accordingly, we used a thinning approach (60 km) to reduce the redundancy among the data.

3. WRF

We simulated Hurricane Harvey using the Weather Research and Forecasting model (WRF) v3.9.1 (Skamarock et al., 2005) in a nested setup encompassing a 27-km outer domain, 9-km and 3-km inner fixed domains for simulation of initial conditions at the landfall, and a 1-km domain for the sensitivity of precipitation to aerosols. The period of simulation is from 23th to 28th August 2017. The parent domain consisted of 120 west-east, 120 south-north grids and 30 vertical pressure sigma levels covering the Gulf of Mexico, Mexico and some portions of the U.S. The nested domains are centered over the Southeast Texas in which the hurricane landed and released most of its energy through precipitation. The initial and lateral boundaries for the parent domain are provided by the National Centers for Environmental Prediction North American Regional Reanalysis (NARR) with a 32 km and 3 h spatial and temporal resolutions (Mesinger et al., 2006), respectively. The boundary conditions for nested domains are provided by their outer domains. All domains are shown in the center of the diagram in Fig. 1.

Since two out of the four domains (d01 and d02 in Fig. 1) are not spatially fine enough to resolve sub-grid clustered convections through exchanging moisture, heat and momentum fluxes between clouds and the environment, we used Betts-Miller-Janic (BMJ) sub-grid cumulus parameterization (Janjić, 1994). This option was shown to reasonably simulate precipitation from Hurricane Rita, its landfall time and track (Nasrollahi et al., 2012). The other domains (d03 and d04) do not require a sub-grid cloud parameterization, as the fluxes are explicitly resolved using the microphysics scheme. We used the Yonsei University (YSU) scheme for the planetary layer fluxes because it produces the intensity of hurricane relatively better than 1.5 and 2.5 order closures in the present study. The Noah Land-Surface Model for the surface physics, and the Rapid Radiative Transfer Model (RRTM) for short- and long-wave radiation are used. There are two surface layer options intended exclusively for Hurricane studies (Davis et al., 2008). First, the drag coefficient in the shear stress at the surface over the ocean is set to a constant value (~0.003) for high wind speeds (Black et al., 2007), which is lower than the default value in the WRF model. As a result of a lower drag, we expected to have stronger winds, higher central pressures, and a wider eyewall radius. Second, we consider the ocean temperature (negative) feedback using a 1-D mixed layer ocean model (Pollard et al., 1972) with 30 m mixing height and 0.03 K m^{-1} lapse rate. Emanuel et al. (2004) suggested that this oversimplified treatment can still account for the first approximation of this feedback.

The formulation of microphysics plays a central role in most of interactions occurring in cloud hydrometeors in the atmosphere (Khain

et al., 2015). We choose not to use any bulk microphysical parametrization scheme despite their computational efficiency as these schemes tend not to be as nearly sensitive as the SBM to aerosol concentration (Fan et al., 2016 and the references therein; Shpund et al., 2019); hence, we used the FAST-SBM scheme (Khain et al., 2009), which rigorously determines the size and number of cloud hydrometeors in four size distributions: aerosols serving as CCN, cloud/rain droplets, aggregates (snow/ice) and graupel/hail. For each group, a logarithmically equidistant doubling mass grid spectrum containing 33 mass bins (for each hydrometeor) is defined in a way that the mass in the $(i + 1)$th bin is twice as large as that in the ith bin. The first and last bins correspond to 2 μm and 4 mm radius drops, respectively. The original format of this scheme follows the concentration of activated CCN from the Twomey activity spectrum equation written as $N_{CCN} = N_0 S_w{}^k$, where N_{CCN} (cm^{-3}) is the number of activated CCN under a particular ambient supersaturation S_w (%); N_0 (cm^{-3}) and k are empirical values indirectly explaining the aerosols properties (Twomey, 1959). Twomey's equation is straightforward because it approximates the CCN spectrum using two variables; however, it does not explicitly take into account some physical constraints such as surface tension and solubility, Thus it is difficult to more specifically specify aerosol characteristics that are dependent on these parameters through setting N_0 and k.

Instead, we specified the location-dependent characteristics of aerosols based on the Goddard Earth Observing System (GEOS)-Chem (geos-chem.org) global, chemical-transport model with the online sectional aerosol microphysics model, TwO Moment Aerosol Sectional (TOMAS) (Adams and Seinfeld, 2002). We used GEOS-Chem-TOMAS v10 with the tropospheric chemistry mechanism (NO$_x$-O$_x$-HC-Aer-Br) plus the TOMAS aerosol microphysics scheme in a $2.0^{\circ} \times 2.5^{\circ}$ spatial resolution. The vertical profiles consisted of 47 eta layers from the surface to 80 km. We used 19 months of simulation prior to the August 2017 for spin-up. The particle phase concentrations were treated in 15 size bins ranging from 3 nm to 10 μm for eight aerosol species, namely as, sulfate, sea salt, dust, aerosol particle water, black, and organic carbon (with hydrophilic and hydrophobic populations for each carbonaceous type). Our assumed hygroscopic factors and densities for each species are discussed elsewhere (Kodros and Pierce, 2017). A more detailed description of the model and its inputs can be found in Kodros et al. (2016).

To translate the GEOS-Chem-TOMAS aerosol information to the FAST-SBM microphysics, we applied several modifications to the FAST-SBM as follows: i) to account for coarser particles from the chemical transport model, we expanded the largest dry particle size from 2 μm to 10 μm, ii) we transferred three dimensional variables of solubility, dry radius grids, aerosol-specific mass and total number of aerosols at each bin from GEOS-Chem-TOMAS to the scheme, and iii) we redesigned the nucleation subroutine to be able to compile the aforementioned information. These modifications removed the dependency of the model on the empirical Twomey's equation. Under the assumption that the particles in each size bin are internally mixed, we calculated the critical saturation ratio at the lower ($S_{low}{}^*$) and upper ($S_{up}{}^*$) boundaries of each bin based on Köhler theory. We then compared the ambient supersaturation from the WRF (S_w) to $S_{low}{}^*$ and $S_{up}{}^*$. Under the criteria of $S_w > S_{low}{}^*$, all aerosol particles are instantly converted to cloud droplets. Under the criteria of $S_w > S_{up}{}^*$, we used the following equation (Gao et al., 2016):

$$N_{CCN} = N_k \times \frac{lnS - ln S_{low}^*}{ln S_{up}^* - ln S_{low}^*} \tag{1}$$

Where N_k is the number of aerosol particles at specific grid cell. If S_w was smaller than the critical saturation ratios, no nucleation was done. All the information transferred from GEOS-Chem-TOMAS to the SBM was predefined across all the domain, meaning that GEOS-Chem-TOMAS is decoupled from the SBM (i.e., one way). Within the SBM, the

predefined aerosols fields were updated with time and space through the activation cloud droplets, diffusion growth/evaporation, and advection. We assumed that the source of aerosols only came from the time-varying boundaries in the largest domain (d01).

3.1. Data assimilation

To improve our high-dimensional numerical representation of Hurricane Harvey, we used an hourly cycling assimilation. We used the WRF model with 3D variational assimilation (3Dvar) (Barker et al., 2004, 2012). This model is originally decoupled from the WRF model; thus, we implemented a shell-file coupler to be able to bridge these two components. WRF-3Dvar seeks to solve the following cost function under the assumption that i) both observation and background error covariances follow Gaussian probability density functions with a zero bias, ii) the observation and background error covariances are independent and iii) the relationship between observation and background can be approximated linearly:

$$J(\mathbf{x}) = (\mathbf{y} - H\mathbf{x})^T (\mathbf{E} + \mathbf{F})^{-1} (\mathbf{y} - H\mathbf{x}) + (\mathbf{x} - \mathbf{x}^b)^T \mathbf{B}^{-1} (\mathbf{x} - \mathbf{x}^b) \tag{2}$$

where $\mathbf{x}$ is the analysis (the a posteiori) given two sources of data: the background ($\mathbf{x}^b$) and observations (y). $\mathbf{F}$, the representative error covariance matrix, denotes the errors induced by H used to transform the analysis space into the observation space. $\mathbf{E}$ and $\mathbf{B}$ are the error covariance matrices of the observations (instrument) and the background (model). The first term of the Eq. (2) attempts to reduce the distance between observations and the estimated values. The second term incorporates some prior understandings and expectations about the true state of the atmosphere, that is, it does not allow the analysis to deviate largely from the background (forecast), even though the observations could be far from estimated. The weight of each term is dictated by its covariance matrix. If $\mathbf{B}$ is too large compared to $\mathbf{E}$, the analysis will be independent of the prior knowledge (background) and, conversely, if $\mathbf{E}$ dominates, the final solution will consist mostly of the a priori. While the instrumental errors are rather well-characterized, a precise knowledge of errors in the background, which is domain-dependent, is unknown. We carried out the 24 and 12 h forecast for every day of the month of August to approximate $\mathbf{B}$ using the National Meteorological Center (NMC) method (Parrish and Derber, 1992). To be able to efficiently use the approximated $\mathbf{B}$ for the variational data assimilation system, four control variables ($\mathbf{v}$) including zonal and meridional winds, temperature, surface pressure, and relative humidity were defined through the relationship $\mathbf{x} - \mathbf{x}^b = \mathbf{U}\mathbf{v}$. The $\mathbf{U}$ transform represents several stages of covariance modeling that has been fully described elsewhere (Barker et al., 2004). Given a reasonably defined $\mathbf{U}$, $\mathbf{U}\mathbf{U}^T$ estimates $\mathbf{B}$ values that can directly be used for the system. The cost function, which is a quadratic equation, is iteratively minimized in an hourly window through the conjugate gradient method. On an hourly basis, we re-initialized the data assimilation 5 times and minimized iteratively the cost function with a maximum number of iteration of 200 using the coagulate gradient method.

4. Brief description of Hurricane Harvey

Similar to the majority of Atlantic tropical cyclones, Hurricane Harvey originated from a westerly wave over Africa passing through to the east of Windward Island under favorable synoptic conditions (Fig. 2). Harvey was not believed to pose a noticeable threat to coastal areas due to the poorly organized structure until late August 23, when it rapidly intensified mainly as a result of excessive heat ocean capacity in the Gulf of Mexico (Trenberth et al., 2018), weak wind shear, high mid-level moisture, and favorable synoptic conditions. At this stage, official forecast models including National Hurricane Center forecast, the ECMWF, and UKMET, all well-predicted the track within margins of error significantly lower than those for the 2012–2017 period; on the other hand, they severely underpredicted the Harvey's intensity by a
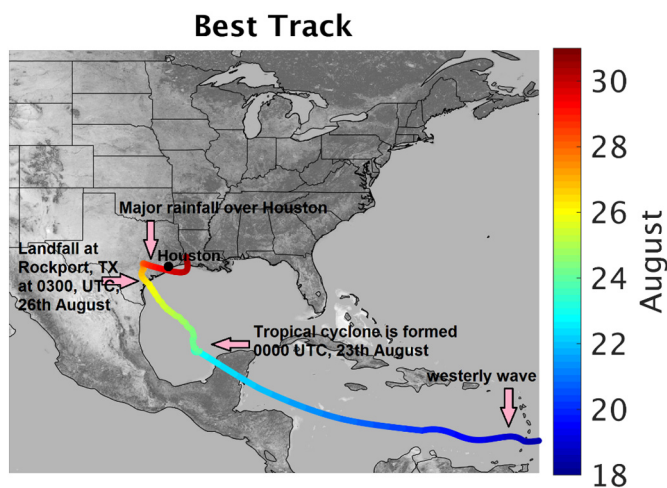
Best Track

Fig. 2. Best track (determined by the National Hurricane Center) of Hurricane Harvey during the period of 18th August to 31st August 2017. The hurricane's minimum pressure and maximum low-level winds were seen as 937 hPa and 59 m/s at 0030 UTC 26 August. The initial time for the numerical modeling of this phenomenon is 0000 UTC 23 August in our study.

factor of two (Blake and Zelinsky, 2018). Harvey reached its maximum intensity at 0030 UTC 26 August and made landfall on Rockport, Texas, with sustained winds of ~ 59 m/s, and a minimum central pressure of 937 hPa.

After it made landfall, the northwestward motion of the hurricane slowed and stalled for more than a day. At this point, the hurricane was sustained by continual moisture flux from the Gulf acting as an effective convective storm generator producing record-breaking rainfall over Houston.

5. Experiments

We first reproduced Hurricane Harvey at landfall and then began our forecasts with two aerosol scenarios. To provide reasonable initial values for the forecasts, we first assimilated the observations in an attempt to prevent the model from diverging from the truth, and second, we nudged the meteorological fields toward a well-characterized large-scale model (here NARR). We conducted four experiments to investigate to what extent deploying assimilation and grid nudging is helpful at reproducing the hurricane properties, namely, as CTRL (neither assimilation nor nudging), SN (only nudging), SDA (only assimilation), and SNDA (both assimilation and nudging). The simulation starts at 0000 UTC 23 August, the time when the tropical cyclone was formed and ends at the landfall at 0030 UTC 26 August. A summary of these scenarios is listed in Table 1.

To quantify the response of Hurricane Harvey to anthropogenic-derived aerosols, we continued performing the simulation from the landfall to 1200 UTC 27 August in all four domains including the high-resolution 1-km domain. We detached the model from the observational constraint but left the nudging on for the first domain (d01). We named

the two scenarios with anthropogenic emissions on/off as SP(polluted)/SC(clean).

6. Results and discussion

6.1. Experimental results from Hurricane Harvey

As noted above, Hurricane Harvey had an observed maximum wind speed of 59 m/s and a minimum pressure of 937 hPa at 0030 UTC 26 August. The left panel of Fig. 3 displays the performance of the model at the 3-km domain resolution (d03) at the observed landing time from CTRL, SN, SDA, and SNDA. To ascertain the structure of the hurricane, we qualitatively used the outgoing longwave radiation (OLR) (a proxy for clouds/convection) and the radar reflectivity. The right panel depicts the best track along with the radar reflectivity in Corpus Christi, Texas. Starting from 0000 UTC 23 August, the CTRL experiment predicts the hurricane landing time one day early. The spatial distribution of track was scattered indicating that the structure of the hurricane is poorly modeled. The intensity of the hurricane in terms of maximum low-level wind speeds and the sea-level pressure barely reached above 25 m/s and falls below 1000 hPa, respectively. In this simulation, the initial and boundary conditions are far too undefined to reproduce the observations of Hurricane Harvey.

We reran the model with nudging toward the NARR reanalysis data (the SN case) given that the data were constrained by observations. The errors in movement and landing time were much reduced. However, the use of reanalysis data results in a large underestimation of the intensity, consistent with Zick and Matyas (2015) who validated the performance of the NARR data in reproducing > 65 tropical cyclones that made landfall in the U.S. during 1998–2012. The underprediction of intensity of those storms were found to be large, mainly as the result of the insufficiency of the NARR spatial resolution to be able to resolve non-hydrostatic components.

We then assimilated the aforementioned observations by numerically solving the cost function in a full-cycle hourly framework. Although the cost function varies by time, on average, the highest values belong to the sounding data suggesting that the largest discrepancy between the model and the observations occurs in the vertical structure of the atmosphere (not shown). During the entire period of simulation, the initial cost function was roughly being reduced by > 50% depending on the availability of observations. After incorporating the observations, certain aspects of the hurricane were more realistically captured. For instance, the vortex structure was fairly well simulated according to the OLR and the radar reflectivity. The severe under-representation of Harvey's intensity from the former scenarios was substantially reduced. The biases of maximum wind speed and minimum sea level pressure were found to be 13 m/s and 23 hPa. The track on the other hand was inferior compared to that of the SN case (~ 100 km). It seems that the relatively small size of our domain undermined the WRF-3Dvar ability to accurately represent the large-scale atmospheric environment. To compensate for the above limitation, we nudged the model toward the NARR for the parent domain (d01). The last panel of Fig. 3 demonstrates that SNDA, which benefited from the combination of the observations and the reanalysis data, beats all
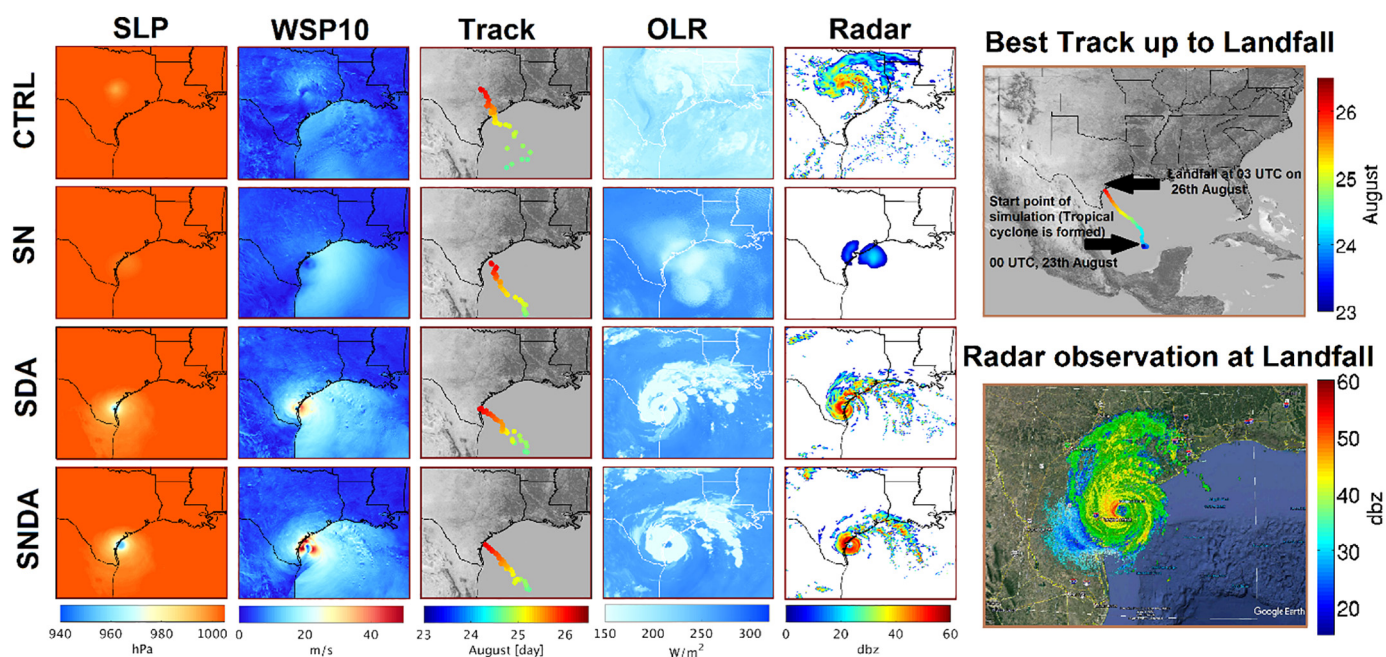
Table 1
The experiments designed to reproduce Harvey at landfall and conduct the sensitivity test in respect with aerosols, namely, as CTRL (neither assimilation nor nudging), SN (only nudging), SDA (only assimilation), SNDA (both assimilation and nudging), SP (with anthropogenic emissions on), and SC (without anthropogenic emissions).

Experiment	Period (UTC)	Grid Nudging (d01, d02, d03, d04)	DA (d01, d02, d03, d04)
CTRL	08/23 00:00-08/26 03:00	off, off, off, N/A	off, off, off, N/A
SN	08/23 00:00-08/26 03:00	on, on, on, N/A	off, off, off, N/A
SDA	08/23 00:00-08/26 03:00	off, off, off, N/A	on, on, on, N/A
SNDA	08/23 00:00-08/26 03:00	on, on, off, N/A	on, on, on, N/A
SP/SC	08/26 03:00-08/27 12:00	on, off, off, off	off, off, off, off

Fig. 3. The left panel shows the simulated sea level pressure (SLP), the wind speed at 10 m (WSP10), the track, outgoing long radiation (OLR) and radar reflectivity on 26th August 2017 at 0300 UTC, when Harvey made a landfall. The right panel demonstrates the best track and the observed radar at the landfall. The SNDA depicted the properties of Harvey more realistically than the other scenarios.

individual experiments. The results obtained in this study suggest that the low spatial coverage (i.e. a regional domain) of the model may have precluded the determination of optimal results, even when ample observations are assimilated in nested domains.

To make an assessment of the overall capability of simulating a set of key aspects of the hurricane, we plotted the time series of maximum wind speed, SLP and track errors for each experiment, shown in Fig. 4. With regard to the wind speed, CTRL and SN cases have relatively constant values. The SDA and SNDA experiments underwent a more rapid intensification after August 25 at a rate of 0.5 m/s per hour resulting in the simulation a major hurricane. Similarly, the middle panel shows that SDA and SNDA consistently performed better than the others with respect to minimum SLP. Concerning the track errors, SDA and SNDA gradually approached closer to the best track after August 24. The reasonable performance of SNDA is promising; judged over all mentioned variables combined it outperformed all individual experiments; therefore we initialized our SC and SP experiments using the physical conditions from this scenario from the landfall.

6.2. Characteristics of aerosols before the landfall

Fig. 5 shows the spatial distribution of daily-averaged mass concentration of five major aerosols on the August 26th over the surface, namely as sulfate, sea salt, black carbon (BC), organic aerosols (OAs) and dust. In general, the less soluble aerosols (e.g., BC, OA and dust) reduce surface tension by reducing the surface curvature. In addition to reducing the curvature effect, soluble aerosols such as sulfate and sea salt, act to reduce the equilibrium vapor pressure of water above the activating droplet, which in turn, can significantly increase the water droplet radius (i.e., the solution effect) (Tao et al., 2012).

The natural sources of sulfate are predominantly from volcanic activities and oceanic dimethyl sulfide (Bates et al., 1992). Therefore, we observe the enhancements of sulfate over the ocean and active volcanos in Central America (box B). The sources of sulfate mainly originate from the oxidation of the S(IV) family through OH, dissolved O_3 and H_2O_2 (e.g., Souri et al., 2017). The model captured a hemispherically transported plume from East Asia (box A) (Park et al., 2004). The highest concentrations of sulfate close to Harvey are seen in box C mainly from

anthropogenic sources in the western Texas. The data suggest that global anthropogenic-derived sulfate was more than twice as large as the natural sulfate. The simulation shows a large mass of sea salt on the path of Harvey (box D); but sea salt contributes proportionally to few CCN due to its larger mass per particle. Biomass burning activities occurring in Canada contributed largely to BC and OA (box E). Relative to total aerosol mass, negligible BC concentrations are seen close to Harvey's landfall. Simulated dust concentrations remained constant under the two scenarios. A dust plume coming from Africa (box F) did not pass through the Gulf of Mexico. Overall, as Fig. 5 shows, the global anthropogenic emissions contributed mainly to more sulfate and organic aerosol mass in Texas.

To generally understand to what extent aerosols can potentially become cloud droplets, we estimated the CCN spectra using the empirical equation (i.e., $N_{CCN} = N_0 S_w^k$) using the analysis presented in Kodros and Pierce (2017). Fig. 6 shows the spatial distribution of CCN concentrations at 1% supersaturation with and without global anthropogenic emissions on the August 26th. Additionally, the bottom panel of the figure shows the CCN spectra within all grid cells over the surface in the 3-km domain (d03). Elevated CCN under the scenario of no anthropogenic emissions appeared over wildfires in Canada. In addition to the release of several inorganic aerosol precursors (Souri et al., 2017), a large number of organic compounds were emitted from biomass burning into the atmosphere (Wiedinmyer et al., 2011). The ratios of CCN concentrations in the scenario with anthropogenic emissions to those without anthropogenic emissions varied from one (over fires) to two orders of magnitude (over Ohio River Valley with high emissions from power plants and industry). The CCN spectra averaged over the 3-km domain, under the 1% supersaturation ratio, suggest that the anthro-off scenario (SC) only builds up to 80 cm^{-3}. The number of CCN hardly increased above 0.5% supersaturation because of a few number of smaller particles (k of 0.2). On the other hand, the anthropogenic sources (mainly sulfate) largely contributed to CCN concentrations ($\sim$ 850 cm^{-3} at 1% supersaturation) with a relatively higher k value (0.26).
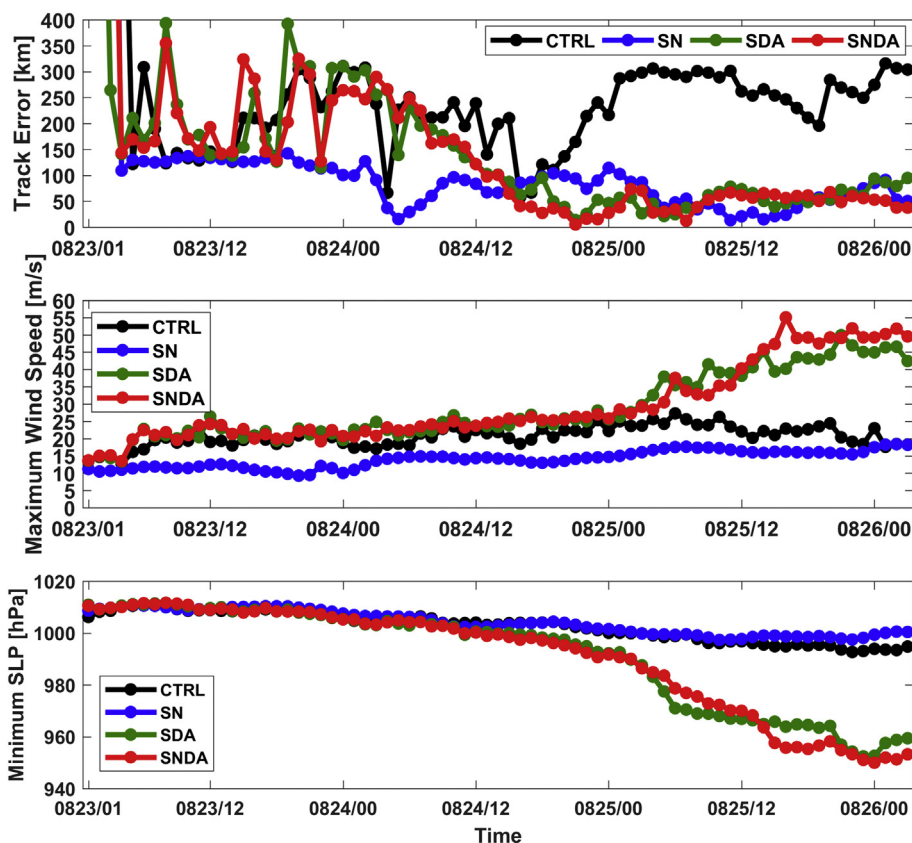
Fig. 4. Time series of the track error (bottom), the maximum wind speed (middle), and the minimum sea level pressure (bottom) for the CTRL, SN, SDA and SNDA experiments from the formation of the storm to the landfall.

6.3. Response of Harvey to anthropogenic aerosols after the landfall

Harvey's record-breaking rainfall was interwoven with two main elements i) a stall over a region inland not too far from the Gulf, and ii)

high ocean heat content present in spite of the negative feedback of the storm on the Gulf (Trenberth et al., 2018). The unusual track of Harvey triggered by a low wind shear permitted the release of excess moisture from the Gulf over Houston. Given the atmospheric conditions from
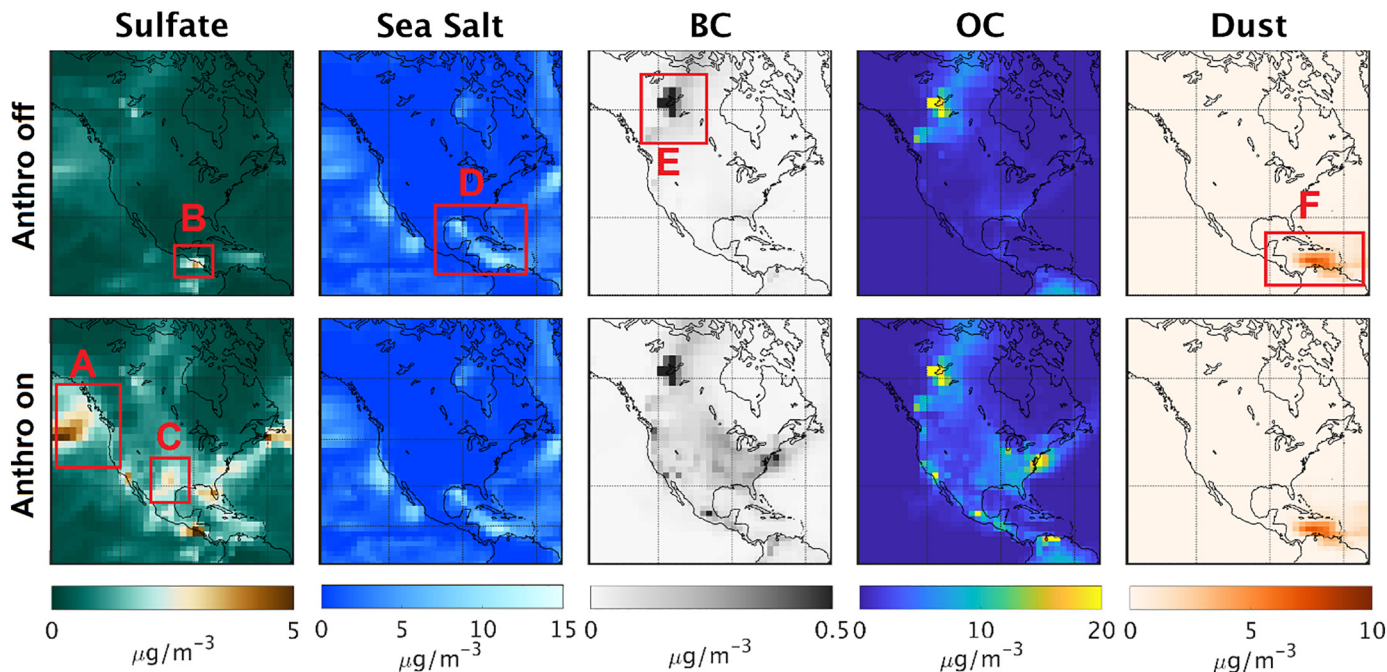
Fig. 5. The mass of five major aerosols simulated by the GEOS-Chem-TOMAS without (first row) and with (second row) global anthropogenic emissions over the surface on 26 August 2017.
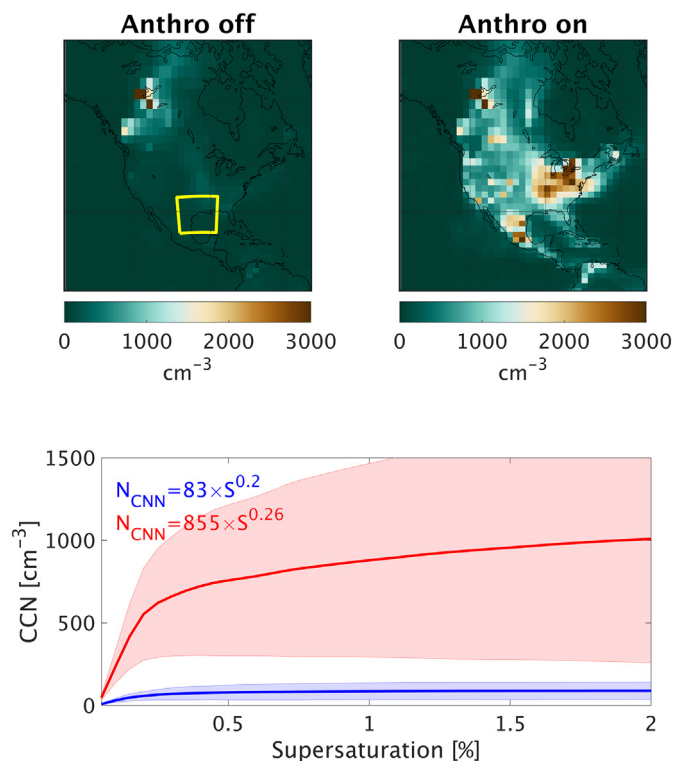
Fig. 6. (top panel) the number of activated aerosols to cloud droplets (CCN) at 1% ambient supersaturation with and without anthropogenic emissions over the surface on August 26. (bottom panel) the fitted CCN spectra based on Twomey's formula on aerosols in the yellow box. Red and blue lines denote cases without and with anthropogenic emissions, respectively. (For interpretation of the references to colour in this figure legend, the reader is referred to the web version of this article.)

both GEOS-Chem-TOMAS and WRF-DA, we continued the simulation by including the 1-km spatial resolution domain (d04) under the two experiments (SC and SP). We identified a negligible difference between the tracks from SC and SP experiments (not shown), as the tracks were mostly driven by large-scale atmospheric conditions. Both scenarios fairly follow the best track within a radius consistently < 50 km.

A number of studies have analyzed the response of precipitation to anthropogenic aerosols (e.g., Khain et al., 2004, 2005; Tao et al., 2007; Fan et al., 2016; Wang et al., 2014; Khain et al., 2015; Khain et al., 2016). Combining the results from former studies suggests that there is no clear correlation between precipitation amounts and aerosols unless we classify the atmospheric environment into moist (i.e., abundant moisture and low wind shear) and dry (i.e., limited moisture and high wind shear) regimes (Tao et al., 2012; Khain et al., 2008). The regimes with Harvey varied with time and space because of the interaction of different environmental scales (from large-scale synoptic conditions to small-scale eddies) governing the dynamic of hurricanes. Likewise, aerosols, along with the physical and chemical processes involved in their formation and loss, changed spatially and temporally.

Fig. 7 shows the simulated water vapor mixing ratio at 2 m, OLR, and the aerosol concentrations at 2 km altitude from the SP experiment in the 1-km domain (d04) starting from 03 UTC 26 August. The largest amount of rainfall over the greater Houston, shown by box G, began shortly after 00 UTC 27 August (~ 20 h after the initial time in the figure). In the first hours of the simulation, we observe that the water mixing ratios in the eyewalls did not differ largely from those over the Gulf. As the eye departed from the Gulf, however, the more moisture it lost. Thick clouds gradually dissipated over the eyewall because of a drier air and mainly mid-level westerly winds (wind shear). The counterclockwise circulation, however, provides a mechanical

mechanism that feeds and prolonged the occurrence of rainbands over Houston. Thus, the atmospheric conditions (shown over box G) were generally moist.

Under dry conditions dictated by either high wind shear or lack of moisture, we expect that enhanced aerosol numbers will generate smaller cloud droplets, resulting in less efficient collision-coalescence that suppresses rainfall. On the other hand, if abundant moisture/latent heat fluxes and low wind shear are present, enhanced aerosol numbers can release the latent heat from water vapor resulting in stronger updrafts and downdrafts. Additionally, a high number of aerosols reduces the size of raindrops at the lower atmosphere causing a stronger evaporative cooling, which in turn, strengthens convergence because of a larger thermal gradient (Tao et al., 2012 and the references therein). The last set of panels within Fig. 7 demonstrates how the aerosol concentrations evolved gradually at 2 km altitude. The anthropogenic aerosol concentrations originating from western Texas near Harvey were carried by a counterclockwise movement of spirals to Houston at the moment when deep convection activity initiated. The concurrent of events underscores the significance of having a chemical transport model accounting for a timely distribution of aerosols.

We computed the differences between the two scenarios with respect to several atmospheric variables including total precipitation (i.e., the amount of rainfall), the liquid water content (LWC), vertical winds (W), and rain mixing ratios. In contrast to previous studies focusing on analyzing this sensitivity in a snapshot, we found that a radial-basis comparison was better able to distinguish the differences between model simulations. We defined an annulus with a fixed thickness of 150 km expanding from the center of the hurricane to beyond 400 km. This annulus scanned the atmospheric fields in increments of 1-km on the right side of the hurricane. We then computed the difference between the two experiments based on the grid cells that fall into the annulus. Fig. 8 shows the radial differences of the aforementioned variables. Around 10 h after the landfall near to the eyewall, we observed an enhancement in vertical winds as strong as 0.05 m/s at 4 km, longer liquid paths, and a higher rain mixing ratio by 0.1 gkg^{-1} at 2 km. These results potentially imply an increase in the release of latent heat attributed to the anthropogenic aerosols passing through the eyewall (the last panel in Fig. 7). Interestingly, the same level of enhancement occurred later at the time in which a narrow band of pollution from the western Texas was transported over the greater Houston (20–24 h after the landfall). The anthropogenic aerosols contributed to the invigoration of deep convection over box G which was associated by an increase in vertical winds and a larger amount of precipitation. However, we noted a reverse trend at those regions located out of box G. This indicates that the enhanced vertical mass flux over Houston dampens convection in further rainbands surrounding the area of most intense convection, mainly a response to the competition between these two regions in the use of moisture/latent fluxes. Therefore, the total amount of precipitation remained unchanged over the entire domain (~ 0.7% difference); but the SP resulted in a heavier rainfall over the greater Houston area on average (~ 25 mm).

Fig. 9 shows the spatial distribution of rainfall in the SC and SP experiments between 0300 UTC 26 August and 1200 UTC 27 August. Not surprisingly, the model and observations indicated a higher amount of rainfall over the land than the ocean because of a larger surface drag coefficient over land that leads to a stronger frictional convergence (i.e., Ekman pumping). Assuming a constant drag coefficient over land, one would expect a higher amount of precipitation on the right side of a hurricane in the Northern Hemisphere because of stronger background winds. Indeed, we observed a larger precipitation amount in the greater Houston area from SP. We attribute this enhancement to an aerosol plume arriving from western Texas at the moment that deep convection initiated over Houston. The average accumulated rainfall during the period over the region of interest was 297 and 322 mm for SC and SP experiments, respectively. In addition to quantifying changes in the simulated Hurricane Harvey precipitation, examining the probability
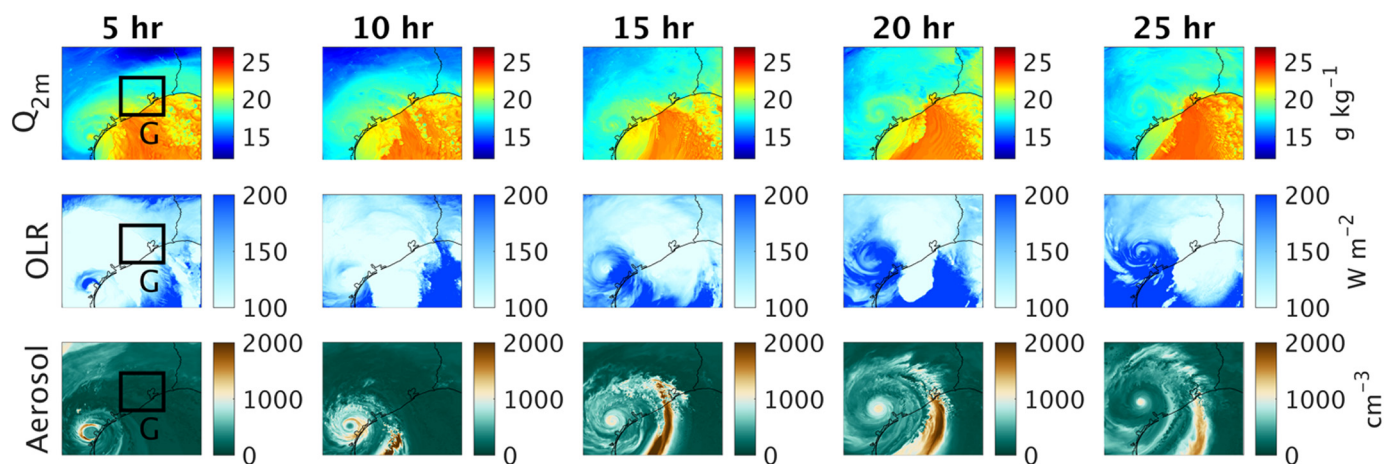
Fig. 7. First row: the simulated water mixing ratio at 2 m, starting from 03 UTC 26 August for the SP experiment. Second row: OLR for detecting the cloud location. Third row: the aerosol concentrations at a 2 km altitude.

distribution of the difference between SP and SC experiments over the greater Houston area is beneficial. Fig. 10 shows the distribution of the differences between SP and SC experiments over the box G, overplotted with a fitted Gaussian function (r^2 = 0.95). The fitted function is shifted by 27 mm toward more positive values suggesting that the number of grid cells with high precipitation amounts were enhanced by the anthropogenic-derived aerosols. In addition, we found a second peak at the right tail of the distribution indicating an increase in the number of grid cells with extremely high rainfall.

7. Summary

Predominantly high ocean heat content and a lack of strong wind shear resulted in a fairly isolated Hurricane Harvey (2017) in Texas (Trenberth et al., 2018). Harvey provoked spatially-compact deep convection over the greater Houston area, producing a national record-breaking rainfall (Emanuel, 2017; Risser and Wehner, 2017). Not only were atmospheric conditions favorable but an abundance of anthropogenic particles that modulated the spatial and temporal distribution

of moisture release was also present. To study these effects, we set up a high-resolution model that is relatively responsive to aerosols, along with a chemical transport model that is capable of accounting for the chemical and physical processes involved in the formation and loss of gases/particles.

Motivated by the need for the quantification of the impact of anthropogenic-derived aerosols on the magnitude of precipitation produced by Harvey, this study rigorously i) reproduced both the chemical and the physical conditions of the atmosphere at landfall, ii) calculated the activation of aerosols explicitly using a spectral bin microphysics scheme, and iii) investigated the changes in precipitation with and without anthropogenic emissions.

In order to reproduce Harvey's properties from when it was formed on 0000 UTC 23 August 2017 up to the time it made a landfall on 0030 UTC 26 August, we assimilated a wide range of data encompassing dropsondes, microwave satellite radiance, GPS refractivity, surface and aircraft observations, into a parent domain (27-km), along with two nested domains (9-km and 3-km) in a full-cycle hourly 3-D variational framework. We found that the cost function derived from Bayes'
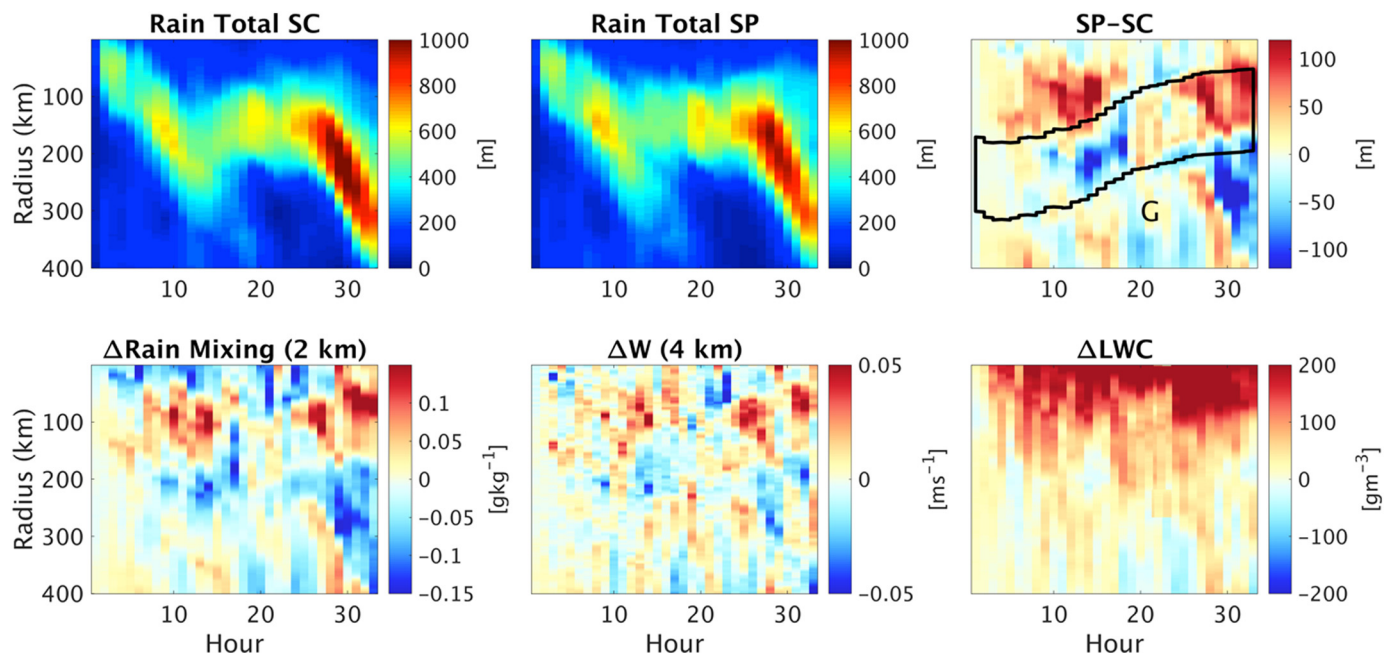

Fig. 8. The radial-basis comparison of the SC and SP experiments for 35 h from the landfall. Total precipitation was estimated by the sum of precipitation at a given radius of the scanning ring. The delta (Δ) denotes the difference between SP and SC for the target variable.
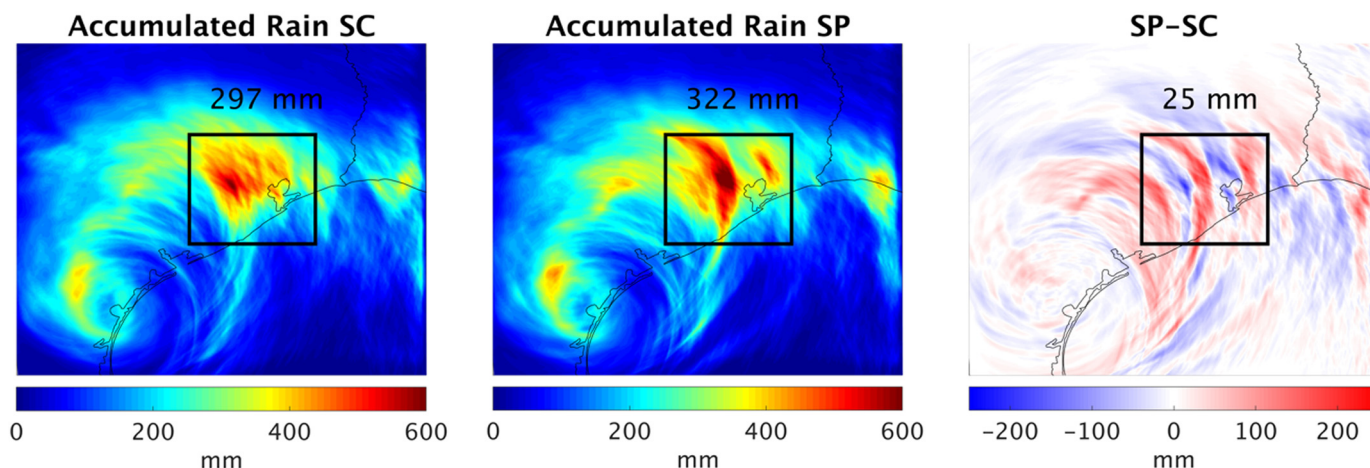
Fig. 9. From left to right: accumulated rainfall during the simulation (0300 UTC 26 August-1200 UTC 27 August) using SC, and SP, and their difference.
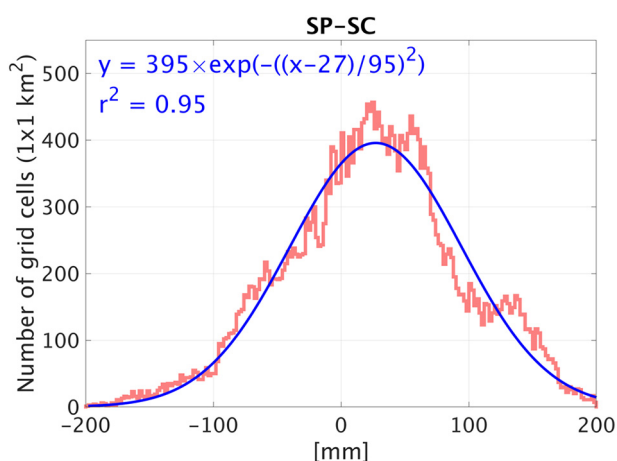

Fig. 10. The histogram of the difference between SP and SC rainfall values over the greater Houston area from 0300 UTC August 26th to 1200 UTC August 27th 2017. The blue line donates the fitted Gaussian distribution. (For interpretation of the references to colour in this figure legend, the reader is referred to the web version of this article.)

theorem used for the assimilation was large for sounding measurements, indicating that the model had a poor performance at the vertical structure of the atmosphere which was improved by the data. We found that the assimilation of the data (for all domains) in conjunction with the NARR reanalysis data (only the parent domain) led to a reasonable performance with regard to track error (48 km), SLP (953 hPa) and maximum wind speed (50 m/s) variables.

To examine the properties of Harvey after landfall, we used the simulated anthropogenic and natural aerosol fields from GEOS-Chem-TOMAS, a chemical-transport model with online aerosol microphysics. Sulfate was the major compound formed from the anthropogenic emission sources in the vicinity of Harvey. Close to Harvey's landfall, the number concentration of CCN with anthropogenic emissions included was found to be an order of magnitude (855 cm^{-3}) larger than those simulated with only natural emissions under 1% ambient supersaturation. We modified the SBM microphysics to nucleate aerosols based on their dry sizes, solubility and concentrations provided by GEOS-Chem-TOMAS under an assumption of the internally-mixed aerosol. A comparison of the simulations with and without anthropogenic emissions showed that precipitation amounts were sensitive to the aerosol loadings; the simulation with anthropogenic aerosols led to stronger vertical winds, the invigoration of deep convective clouds, and heavier rainfall at times when polluted airmasses passed through. Specifically, at the peak of precipitation over Houston, a narrow band of

elevated aerosol was transported over the region from western Texas, which accelerated updrafts/downdrafts thereby enhancing the catastrophic rainfall by 8% (25 mm) on average. Although directly comparing the amount of changes in precipitation from this study to that of former ones might not be feasible because of the differences among microphysics scheme used, properties of aerosols, and the dynamical aspects of the target (e.g., hurricane, squall lines, super cells and etc.), the 8% increase in box G precipitation is in good agreement with a study done by Li et al. (2009); they found a 13% enhancement in precipitation in for a squall line under a polluted scenario ($\sim$ 2000 cm^{-3}) using a two-moment bulk microphysical scheme. We observed a second peak at right tail of the distribution of differences between SP and SC experiments which is an indication of having more extreme rainfall over Houston. We speculate that the additional rainfall due to aerosol incursion can have important implications for flood risk management.

The findings from this study demonstrate that human-made particles, predominantly in the form of sulfate, partly dictated the distribution of heat and the release of moisture during the event. State-of-the-art weather and chemical models used suggest that atmospheric pollutants made by human can be partly responsible for the severity of weather.

Declaration of Competing Interest

The authors declare that they have no known competing financial interests or personal relationships that could have appeared to influence the work reported in this paper.

References

Adams, P.J., Seinfeld, J.H., 2002. Predicting global aerosol size distributions in general circulation models. J. Geophys. Res. 107 https://doi.org/10.1029/2001JD001010. AAC 4-1-AAC 4-23.

Albrecht, B.A., 1989. Aerosols, cloud microphysics, and fractional cloudiness. Science 245, 1227–1230. https://doi.org/10.1126/science.245.4923.1227.

Anthes, R.A., Bernhardt, P.A., Chen, Y., Cucurull, L., Dymond, K.F., Ector, D., Healy, S.B., Ho, S.-P., Hunt, D.C., Kuo, Y.-H., Liu, H., Manning, K., McCormick, C., Meehan, T.K., Randel, W.J., Rocken, C., Schreiner, W.S., Sokolovskiy, S.V., Syndergaard, S., Thompson, D.C., Trenberth, K.E., Wee, T.-K., Yen, N.L., Zeng, Z., 2008. The COSMIC/FORMOSAT-3 Mission: early results. Bull. Am. Meteorl. Soc. 89, 313–334. https://doi.org/10.1175/BAMS-89-3-313.

Auligné, T., McNally, A.P., Dee, D.P., 2007. Adaptive bias correction for satellite data in a numerical weather prediction system. Q. J. R. Meteorol. Soc. 133, 631–642. https://doi.org/10.1002/qj.56.

Barker, D.M., Huang, W., Guo, Y.-R., Bourgeois, A.J., Xiao, Q.N., 2004. A three-dimensional variational data assimilation system for MM5: implementation and initial results. Mon. Wea. Rev. 132, 897–914. https://doi.org/10.1175/1520-0493(2004)132<0897:ATVDAS>2.0.CO;2.

Barker, D., Huang, X.-Y., Liu, Z., Auligné, T., Zhang, Xin, Rugg, S., Ajjaji, R., Bourgeois, A., Bray, J., Chen, Y., Demirtas, M., Guo, Y.-R., Henderson, T., Huang, W., Lin, H.-C., Michalakes, J., Rizvi, S., Zhang, Xiaoyan, 2012. The weather research and forecasting model's community variational/ensemble data assimilation system: WRFDA. Bull. Am. Meteorl. Soc. 93, 831–843. https://doi.org/10.1175/BAMS-D-11-00167.1.

Bates, T.S., Lamb, B.K., Guenther, A., Dignon, J., Stoiber, R.E., 1992. Sulfur emissions to the atmosphere from natural sources. J. Atmos. Chem. 14, 315–337. https://doi.org/10.1007/BF00115242.

Bedka, K.M., Mecikalski, J.R., 2005. Application of satellite-derived atmospheric motion vectors for estimating mesoscale flows. J. Appl. Meteorol. 44, 1761–1772. https://doi.org/10.1175/JAM2264.1.

Black, P.G., D'Asaro, E.A., Drennan, W.M., French, J.R., Niiler, P.P., Sanford, T.B., Terrill, E.J., Walsh, E.J., Zhang, J.A., 2007. Air–sea exchange in Hurricanes: synthesis of observations from the coupled boundary layer air–sea transfer experiment. Bull. Am. Meteorl. Soc. 88, 357–374. https://doi.org/10.1175/BAMS-88-3-357.

Blake, E.S., Zelinsky, D.A., 2018. Hurricane Harvey. National Hurricane Center Tropical Cyclone Rep. AL092017. https://www.nhc.noaa.gov/data/tcr/AL092017_Harvey.pdf.

Davis, C., Wang, W., Chen, S.S., Chen, Y., Corboserio, K., DeMaria, M., Dudhia, J., Holland, G., Klemp, J., Michalakes, J., Reeves, H., Rotunno, R., Snyder, C., Xiao, Q., 2008. Prediction of landfalling Hurricanes with the advanced Hurricane WRF model. Mon. Wea. Rev. 136, 1990–2005. https://doi.org/10.1175/2007MWR2085.1.

Emanuel, K.A., 1986. An air-sea interaction theory for tropical cyclones. Part I: steady-state maintenance. J. Atmos. Sci. 43, 585–605. https://doi.org/10.1175/1520-0469(1986)043<0585:AASITF>2.0.CO;2.

Emanuel, K.A., 1987. The dependence of hurricane intensity on climate. Nature 326, 483–485. https://doi.org/10.1038/326483a0.

Emanuel, K., 2017. Assessing the present and future probability of Hurricane Harvey's rainfall. PNAS 114, 12681–12684. https://doi.org/10.1073/pnas.1716222114.

Emanuel, K., DesAutels, C., Holloway, C., Korty, R., 2004. Environmental control of tropical cyclone intensity. J. Atmos. Sci. 61, 843–858. https://doi.org/10.1175/1520-0469(2004)061<0843:ECOTCI>2.0.CO;2.

Fan, J., Wang, Y., Rosenfeld, D., Liu, X., 2016. Review of aerosol–cloud interactions: mechanisms, significance, and challenges. J. Atmos. Sci. 73, 4221–4252. https://doi.org/10.1175/JAS-D-16-0037.1.

Ferraro, R.R., Weng, F., Grody, N.C., Zhao, L., 2000. Precipitation characteristics over land from the NOAA-15 AMSU sensor. Geophys. Res. Lett. 27, 2669–2672. https://doi.org/10.1029/2000GL011665.

Gao, W., Fan, J., Easter, R.C., Yang, Q., Zhao, C., Ghan, S.J., 2016. Coupling spectral-bin cloud microphysics with the MOSAIC aerosol model in WRF-Chem: methodology and results for marine stratocumulus clouds. J. Adv. Modeling Earth Syst. 8, 1289–1309. https://doi.org/10.1002/2016MS000676.

Garrett, T.J., Zhao, C., 2006. Increased Arctic cloud longwave emissivity associated with pollution from mid-latitudes. Nature 440, 787–789. https://doi.org/10.1038/nature04636.

Hartmann, D.L., et al., 2010. Climate change 2013: The physical science basis. In: Stocker, T.F. (Ed.), Contribution of Working Group I to the Fifth Assessment Report of the Intergovernmental Panel on Climate Change. Cambridge Univ. Press, Cambridge, pp. 159–254.

Janjić, Z.I., 1994. The Step-Mountain Eta coordinate model: further developments of the convection, viscous sublayer, and turbulence closure schemes. Mon. Wea. Rev. 122, 927–945. https://doi.org/10.1175/1520-0493(1994)122<0927:TSMECM>2.0.CO;2.

Jung, J., Souri, A.H., Wong, D.C., Lee, S., Jeon, W., Kim, J., Choi, Y., 2019. The impact of the direct effect of aerosols on meteorology and air quality using aerosol optical depth assimilation during the KORUS-AQ Campaign. J. Geophys. Res. 124, 8303–8319. https://doi.org/10.1029/2019JD030641.

Khain, A., Pokrovsky, A., Pinsky, M., Seifert, A., Phillips, V., 2004. Simulation of effects of atmospheric aerosols on deep turbulent convective clouds using a spectral microphysics mixed-phase cumulus cloud model. Part I: model description and possible applications. J. Atmos. Sci. 61, 2963–2982. https://doi.org/10.1175/JAS-3350.1.

Khain, A., Rosenfeld, D., Pokrovsky, A., 2005. Aerosol impact on the dynamics and microphysics of deep convective clouds. Q. J. R. Meteorol. Soc. 131, 2639–2663. https://doi.org/10.1256/qj.04.62.

Khain, A., Cohen, N., Lynn, B., Pokrovsky, A., 2008. Possible aerosol effects on lightning

activity and structure of Hurricanes. J. Atmos. Sci. 65, 3652–3677. https://doi.org/10.1175/2008JAS2678.1.

Khain, A.P., Leung, L.R., Lynn, B., Ghan, S., 2009. Effects of aerosols on the dynamics and microphysics of squall lines simulated by spectral bin and bulk parameterization schemes. J. Geophys. Res. 114. https://doi.org/10.1029/2009JD011902.

Khain, A.P., Beheng, K.D., Heymsfield, A., Korolev, A., Krichak, S.O., Levin, Z., Pinsky, M., Phillips, V., Prabhakaran, T., Teller, A., van den Heever, S.C., Yano, J.-I., 2015. Representation of microphysical processes in cloud-resolving models: Spectral (bin) microphysics versus bulk parameterization. Rev. Geophys. 53, 247–322. https://doi.org/10.1002/2014RG000468.

Khain, A., Lynn, B., Shpund, J., 2016. High resolution WRF simulations of Hurricane Irene: Sensitivity to aerosols and choice of microphysical schemes. Atmos. Res. 167, 129–145. https://doi.org/10.1016/j.atmosres.2015.07.014.

Knutson, T.R., McBride, J.L., Chan, J., Emanuel, K., Holland, G., Landsea, C., Held, I., Kossin, J.P., Srivastava, A.K., Sugi, M., 2010. Tropical cyclones and climate change. Nat. Geosci. 3, 157–163. https://doi.org/10.1038/ngeo779.

Kochanski, A.K., Mallia, D.V., Fearon, M.G., Mandel, J., Souri, A.H., Brown, T., 2019. Modeling wildfire smoke feedback mechanisms using a coupled fire-atmosphere model with a radiatively active aerosol scheme. J. Geophys. Res. 124, 9099–9116. https://doi.org/10.1029/2019JD030558.

Kodros, J.K., Pierce, J.R., 2017. Important global and regional differences in aerosol cloud-albedo effect estimates between simulations with and without prognostic aerosol microphysics. J. Geophys. Res. 122, 4003–4018. https://doi.org/10.1002/2016JD025886.

Kodros, J.K., Cucinotta, R., Ridley, D.A., Wiedinmyer, C., Pierce, J.R., 2016. The aerosol radiative effects of uncontrolled combustion of domestic waste. Atmos. Chem. Phys. 16, 6771–6784. https://doi.org/10.5194/acp-16-6771-2016.

Kossin, J.P., 2018. A global slowdown of tropical-cyclone translation speed. Nature 558, 104–107. https://doi.org/10.1038/s41586-018-0158-3.

Kursinski, E.R., Hajj, G.A., Schofield, J.T., Linfield, R.P., Hardy, K.R., 1997. Observing Earth's atmosphere with radio occultation measurements using the Global Positioning System. J. Geophys. Res. 102, 23429–23465. https://doi.org/10.1029/97JD01569.

Li, G., Wang, Y., Lee, K.-H., Diao, Y., Zhang, R., 2009. Impacts of aerosols on the development and precipitation of a mesoscale squall line. J. Geophys. Res. 114. https://doi.org/10.1029/2008JD011581.

Lin, Y., Zhao, M., Zhang, M., 2015. Tropical cyclone rainfall area controlled by relative sea surface temperature. Nat. Commun. 6, 1–7. https://doi.org/10.1038/ncomms7591.

Lu, P., Lin, N., Emanuel, K., Chavas, D., Smith, J., 2018. Assessing Hurricane rainfall mechanisms using a physics-based model: Hurricanes Isabel (2003) and Irene (2011). J. Atmos. Sci. 75, 2337–2358. https://doi.org/10.1175/JAS-D-17-0264.1.

Lynn, B.H., Khain, A.P., Dudhia, J., Rosenfeld, D., Pokrovsky, A., Seifert, A., 2005. Spectral (Bin) microphysics coupled with a mesoscale model (MM5). Part I: model description and first results. Mon. Wea. Rev. 133, 44–58. https://doi.org/10.1175/MWR-2840.1.

Lynn, B.H., Khain, A.P., Bao, J.W., Michelson, S.A., Yuan, T., Kelman, G., Rosenfeld, D., Shpund, J., Benmoshe, N., 2015. The sensitivity of Hurricane Irene to aerosols and ocean coupling: simulations with WRF spectral bin microphysics. J. Atmos. Sci. 73, 467–486. https://doi.org/10.1175/JAS-D-14-0150.1.

Mesinger, F., DiMego, G., Kalnay, E., Mitchell, K., Shafran, P.C., Ebisuzaki, W., Jović, D., Woollen, J., Rogers, E., Berbery, E.H., Ek, M.B., Fan, Y., Grumbine, R., Higgins, W., Li, H., Lin, Y., Manikin, G., Parrish, D., Shi, W., 2006. North American Regional Reanalysis. Bull. Am. Meteor. Soc. 87, 343–360. https://doi.org/10.1175/BAMS-87-3-343.

Nasrollahi, N., AghaKouchak, A., Li, J., Gao, X., Hsu, K., Sorooshian, S., 2012. Assessing the impacts of different WRF precipitation physics in Hurricane simulations. Wea. Forecasting 27, 1003–1016. https://doi.org/10.1175/WAF-D-10-05000.1.

Park, R.J., Jacob, D.J., Field, B.D., Yantosca, R.M., Chin, M., 2004. Natural and transboundary pollution influences on sulfate-nitrate-ammonium aerosols in the United States: Implications for policy. J. Geophys. Res. 109. https://doi.org/10.1029/2003JD004473.

Parrish, D.F., Derber, J.C., 1992. The national meteorological center's spectral statistical-interpolation analysis system. Mon. Wea. Rev. 120, 1747–1763. https://doi.org/10.1175/1520-0493(1992)120<1747:TNMCSS>2.0.CO;2.

Pollard, R.T., Rhines, P.B., Thompson, R.O., 1972. The deepening of the wind-mixed layer. Geophys. Astrophys. Fluid Dyn. 4 (1), 381–404.

Risser, M.D., Wehner, M.F., 2017. Attributable human-induced changes in the likelihood and magnitude of the observed extreme precipitation during Hurricane Harvey. Geophys. Res. Lett. 44, 12,457–12,464. https://doi.org/10.1002/2017GL075888.

Shpund, J., Khain, A., Rosenfeld, D., 2019. Effects of sea spray on the dynamics and microphysics of an idealized tropical cyclone. J. Atmos. Sci. 76, 2213–2234. https://doi.org/10.1175/JAS-D-18-0270.1.

Skamarock, W.C., Klemp, J.B., Dudhia, J., Gill, D.O., Barker, D.M., Wang, W., Powers, J.G., 2005. A Description of the Advanced Research WRF version 2 (No. NCAR/TN-468+ STR). National Center For Atmospheric Research Boulder Co Mesoscale and Microscale Meteorology Div.

Souri, A.H., Choi, Y., Jeon, W., Kochanski, A.K., Diao, L., Mandel, J., Bhave, P.V., Pan, S., 2017. Quantifying the impact of biomass burning emissions on major inorganic aerosols and their precursors in the U.S. J. Geophys. Res. 122, 12,020–12,041. https://doi.org/10.1002/2017JD026788.

Tao, W.-K., Li, X., Khain, A., Matsui, T., Lang, S., Simpson, J., 2007. Role of atmospheric aerosol concentration on deep convective precipitation: cloud-resolving model simulations. J. Geophys. Res. 112. https://doi.org/10.1029/2007JD008728.

Tao, W.-K., Chen, J.-P., Li, Z., Wang, C., Zhang, C., 2012. Impact of aerosols on convective clouds and precipitation. Rev. Geophys. 50. https://doi.org/10.1029/

2011RG000369.

Trenberth, K.E., Cheng, L., Jacobs, P., Zhang, Y., Fasullo, J., 2018. Hurricane Harvey links to ocean heat content and climate change adaptation. Earth's Future 6, 730–744. https://doi.org/10.1029/2018EF000825.

Twomey, S., 1959. The nuclei of natural cloud formation part I: the chemical diffusion method and its application to atmospheric nuclei. Geofisica Pura e Applicata 43, 227–242. https://doi.org/10.1007/BF01993559.

Velden, C., Lewis, W.E., Bresky, W., Stettner, D., Daniels, J., Wanzong, S., 2016. Assimilation of high-resolution satellite-derived atmospheric motion vectors: impact on HWRF forecasts of tropical cyclone track and intensity. Mon. Wea. Rev. 145, 1107–1125. https://doi.org/10.1175/MWR-D-16-0229.1.

Walsh, K.J.E., McBride, J.L., Klotzbach, P.J., Balachandran, S., Camargo, S.J., Holland, G., Knutson, T.R., Kossin, J.P., Lee, T., Sobel, A., Sugi, M., 2016. Tropical cyclones and climate change. Wiley Interdiscip. Rev. Clim. Chang. 7, 65–89. https://doi.org/10.1002/wcc.371.

Wang, Y., Lee, K.-H., Lin, Y., Levy, M., Zhang, R., 2014. Distinct effects of anthropogenic aerosols on tropical cyclones. Nat. Clim. Chang. 4, 368–373. https://doi.org/10.

1038/nclimate2144.

Wang, Y., Zhang, R., Saravanan, R., 2014b. Asian pollution climatically modulates mid-latitude cyclones following hierarchical modelling and observational analysis. Nat. Commun. 5, 1–7. https://doi.org/10.1038/ncomms4098.

Wiedinmyer, C., Akagi, S.K., Yokelson, R.J., Emmons, L.K., Al-Saadi, J.A., Orlando, J.J., Soja, A.J., 2011. The Fire INventory from NCAR (FINN): a high resolution global model to estimate the emissions from open burning. Geosci. Model Dev. 4, 625–641. https://doi.org/10.5194/gmd-4-625-2011.

Yang, X., Zhou, L., Zhao, C., Yang, J., 2018. Impact of aerosols on tropical cyclone-induced precipitation over the mainland of China. Clim. Chang. 148, 173–185. https://doi.org/10.1007/s10584-018-2175-5.

Zhao, C., Lin, Y., Wu, F., Wang, Yang, Li, Z., Rosenfeld, D., Wang, Yuan, 2018. Enlarging rainfall area of tropical cyclones by atmospheric aerosols. Geophys. Res. Lett. 45, 8604–8611. doi:https://doi.org/10.1029/2018GL079427.

Zick, S.E., Matyas, C.J., 2015. Tropical cyclones in the North American Regional Reanalysis: an assessment of spatial biases in location, intensity, and structure. J. Geophys. Res. 120, 1651–1669. https://doi.org/10.1002/2014JD022417.